Interspecies Radiative Transition in Warm and Superdense Plasma Mixtures

S. X. Hu,[1,*] V. V. Karasiev,[1] V. Recoules[2], P. M. Nilson,[1] N. Brouwer,[2] and M. Torrent[2]

[1]Laboratory for Laser Energetics, University of Rochester,

250 East River Road, Rochester, NY 14623-1299, USA

[2] CEA, DAM, DIF, 91297 Arpajon, France

[*]Correspondence and request for materials should be addressed to S.X.H. (Email: shu@lle.rochester.edu)

ABSTRACT

Superdense plasmas widely exist in planetary interiors and astrophysical objects such as brown-dwarf cores and white dwarfs. How atoms behave under such extreme-density conditions is not yet well understood, even in single-species plasmas. Here, we have applied thermal density functional theory to investigate the radiation spectra of superdense iron–zinc plasma mixtures at mass densities of ρ = 250 to 2000 g cm^{-3} and temperatures of kT = 50 to 100 eV, accessible by double-shell–target implosions. Our *ab initio* calculations reveal two extreme atomic-physics phenomena—firstly, an interspecies radiative transition; and, secondly, the breaking down of the dipole-selection rule for radiative transitions in isolated atoms. Our first-principles calculations predict that for superdense plasma mixtures, both interatomic radiative transitions and dipole-forbidden transitions can become comparable to the normal intra-atomic K_α-emission signal. These physics phenomena were

not previously considered for extreme high-density plasma mixtures at super-high energy densities.

Introduction

Extreme material conditions, such as super-high density and warm or hot temperatures, can be widely found in the universe. For example, brown-dwarf cores and white dwarfs[1–3] can have a mass density of $\rho = 10^3$ to 10^7 g cm^{-3} and temperatures up to ~10^6 K. Thanks to technological advancements, such extreme states of matter can now be created in the laboratory using powerful lasers[4–7] and/or pulsed-power machines[8]. For instance, deuterium and tritium contained in a millimeter-size inertial confinement fusion (ICF) target can be squeezed to $\rho = 10^2$ to 10^3 g cm^{-3} by powerful lasers through laser-driven compression and spherical convergence[9–13]. Using double-shell implosions[14,15], mid-/high-*Z* materials can be squeezed to super-high densities ranging from $\rho = 10^3$ to 10^4 g cm^{-3} with a temperature ranging from tens to hundreds of electron volts (1 eV ~ 11,604 K). Understanding how matter behaves at such extreme conditions is the purview of high-energy-density physics, inertial confinement fusion, planetary science, and astrophysics.

Under super-dense conditions, atoms and molecules—the fundamental building blocks of matter—can have drastically different properties from those found under ambient conditions. For instance, because of pressure ionization, the binding energy of core electrons of atoms might significantly shift in dense plasmas[16–18] when compared to the case of isolated atoms. By probing the energy level changes in these systems, one can infer the dense plasma conditions if one knows precisely beforehand how atoms behave in high-density environments. Moreover, such an extreme environment experienced by embedded ions can also alter the characteristics of atomic wave functions because of closely encountered neighboring ions. This can have profound implications for understanding radiation transport in such dense plasmas. For example, the dipole-selection rules for

isolated atoms can break down in extremely dense plasmas. Most interestingly, if a plasma mixture is compressed to very high densities above 10^3 g cm^{-3}, wave-function overlapping of deeply bound electrons between different atomic species may occur. A schematic diagram of such a scenario is depicted in Fig. 1, in which the iron (Fe) and zinc (Zn) ions in the mixture closely interact with each other in superdense plasma. As a result of the short distance (d) between the two species, their outer electrons on n = 3 and n = 4 levels can be pressure ionized and their 2*s* and 2*p* states might also be significantly distorted by each other. The significant overlapping of n = 2 states could enable a physics phenomenon—interspecies radiative transitions (IRT)—to occur.

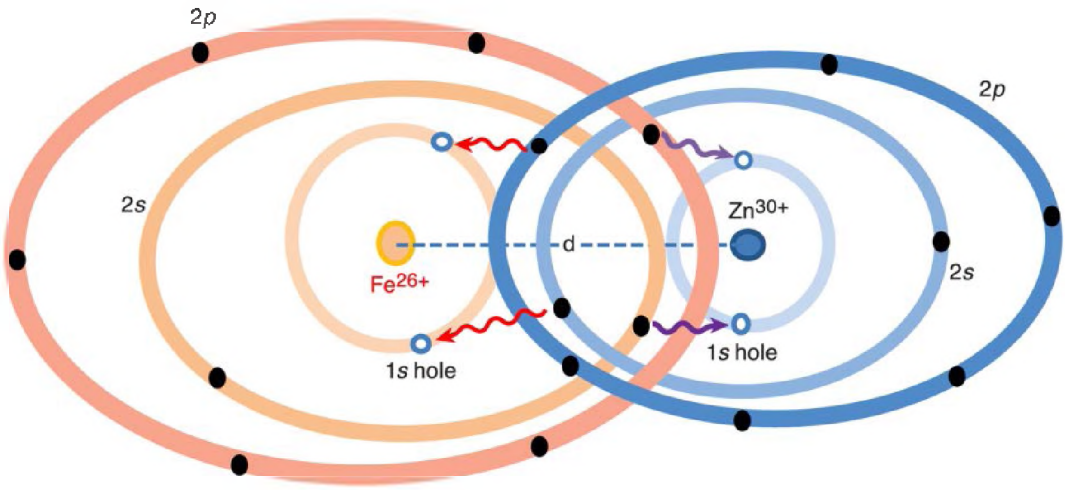

Fig.1 **The schematic diagram of interspecies radiative transition (IRT) in superdense plasmas**. Due to the high compression of superdense plasmas, ions of different species can get so close to each other that their atomic states may become overlapping. In such a superdense environment, photon-pumping or collision-induced 1s-core holes can be filled by 2p electrons from other species, giving rise to inter-atomic K_α emission.

As Fig. 1 illustrates, if 1*s* holes of both Fe and Zn ions are created by either radiation pumping[19] or energetic electron collisions[20,21], the 2*s* and 2*p* electrons of one species

(e.g., Fe) could radiatively transition to the 1*s* hole of the other species (e.g., Zn), giving interspecies K_α emission. On the other hand, if the 2*p* state is no longer fully occupied and the 1*s*-core state is filled, the interspecies K_α absorption could occur in such extremely dense plasma mixtures. To the best of our knowledge, this phenomenon of IRT between bound states has not been considered in emissivity/opacity calculations of plasma mixtures[22–26], even though inter-Coulombic Auger decay was discovered in large molecules and clusters[27–29] and collision-induced absorption and emission between atomic gases was discussed[30–32]. Furthermore, the significant distortion of the 2*s* state resulting from closest neighboring ions will make both intra-atomic and inter-atomic 2*s*–1*s* transitions possible, which are dipole forbidden for an isolated atom and relatively low-density systems when deeply bound 2*s* and 1*s* states preserve their ideal *s* symmetry. To classify various transitions, we use the word of intra-atomic for transitions of electron having both initial state and final state belong to the same atom; while inter-atomic transitions involve two atoms that can be either the same type or different species.

Here, we present interspecies radiative-transition results from first principles calculations by thermal density functional theory (DFT) using the ABINIT software package[33,34] in the plane-wave based projector augmented-wave (PAW) approach. All electrons are considered as evolving -- no frozen core approximation -- and spin-orbit coupling effects are explicitly included. As an example for mid-Z elements presented in brown-dwarf cores, a dense plasma mixture of Fe and Zn was considered with an equal atomic fraction for each species (50:50). We varied the Fe–Zn plasma density from $\rho = 250$ to 2000 g cm^{-3} and temperatures of kT = 50 to 100 eV. For a chosen plasma condition, we first ran orbital-free DFT-based molecular dynamics[35,36] to obtain the equilibrium ionic

configurations. We then took several snapshots of uncorrelated ionic configuration for the electronic structure calculations using ABINIT. Once the electronic structure of a dense plasma is determined from the ABINIT calculations, we created a 1*s*-hole state by removing the occupation of the 1*s* state for both Fe and Zn ions. Finally, we calculated the dipole matrices to determine the emission spectra of superdense Fe–Zn plasmas with the Kubo–Greenwood formalism. More numerical details and convergence tests can be found in the Methods and Supplementary Information.

Results

Interspecies radiative transition in warm and super-dense plasmas. For a superdense and warm Fe–Zn plasma of $\rho = 1000$ g cm^{-3} and kT = 50 eV with 1*s* vacancies of both Fe and Zn ions, the calculated emission coefficient as a function of photon energy is shown by the solid red line in Fig. 2. To identify the IRT features, we also plotted the spectra of single-species Fe (dashed–dotted green line) and Zn (dashed blue line) plasmas in Fig. 2, respectively. Again, these pure plasmas have the same density and temperature conditions as that of the Fe–Zn mixture.

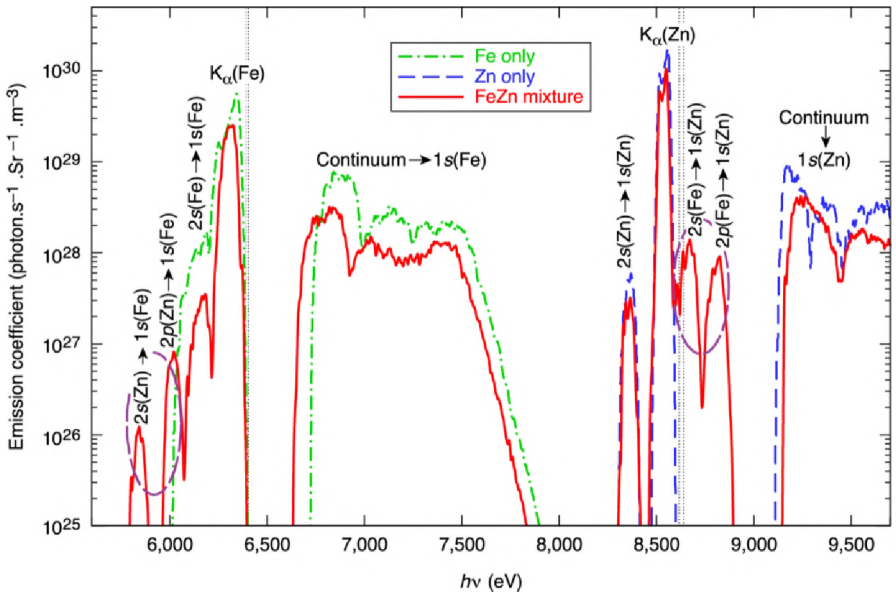

Fig. 2 **The emission spectra of superdense plasmas.** Three cases are calculated for Fe-only, Zn-only, and Fe–Zn mixture having 1*s* vacancy at $\rho = 1000$ g cm^{-3} and kT = 50 eV, using density functional theory (DFT) with ABINIT.

From Fig. 2, one can clearly see that four additional spectral peaks appear in the superdense Fe–Zn plasma mixtures (highlighted by the dashed ellipse): the two emission lines located at $h\nu \approx 8666$ eV and $h\nu \approx 8816$ eV correspond to transitions from the 2*s* and 2*p* states of the Fe ion to the 1*s* hole of the Zn ion, while the other two peaks at $h\nu \approx 5838$ eV and $h\nu \approx 6012$ eV belong to radiative transitions of 2*s*/2*p* electrons of the Zn ion to the 1*s* vacancy of Fe. Besides these interatomic K_α emissions, the dominant intra-atomic K_α lines for each species, are of course, present in the emission spectra in Fig. 2. The vertical dotted black lines mark the normal intra-atomic K_α locations of ambient Fe and Zn, respectively. The red shift of the intra-atomic K_α line is caused by the increased electron screening resulting from the dense plasma environment[19]. In addition, the intra-atomic $2s \rightarrow 1s$ transitions for each species, although being about three orders of

magnitude weaker than the normal intra-atomic K_α lines, also appear as a consequence of the breaking down of the dipole-selection rule due to the density-induced distortion of 2*s* states. Finally, the continuum emissions from free electrons filling 1*s* holes of Fe and Zn ions are also present in the emission spectra, as expected (shown by Fig. 2).

To further understand the emission spectra of Fig. 2, we have computed the density of states (DOS) for the three dense-plasma cases. The results are plotted in Fig. 3, in which Figs. 3(a) and 3(b) are for Fe-only and Zn-only plasmas, respectively. One finds that the outer bound states of 3*s*, 3*p*, 3*d* (or 4*s*) states of Fe and Zn atoms have merged into the continuum because of pressure and thermal ionization. Note that the continuum states below and above the Fermi level (E_F) [i.e., chemical potential] are partially occupied. Clearly, the discrete states of 1*s*, 2*s*, and 2*p* of Fe and Zn ions are evidenced in Figs. 3(a) and 3(b). By looking into the occupations on states below the Fermi energy, the estimated average ionizations are $\langle Z \rangle \approx 17.3$ and $\langle Z \rangle \approx 19.1$, respectively, for Fe-only and Zn-only cases. This indicates that the 2*p* state of Fe begins to be partially occupied. When Fe and Zn plasmas are mixed together, their discrete states of 1*s*, 2*s*, and 2*p* are slightly red/blue shifted by ~15 to 30 eV in Fig. 3(c) when compared to the corresponding pure-plasma cases. This shift can be attributed to the interactions between the two species. Now, if their 1*s* states become empty, *i.e.* a hole/vacancy is created, the radiative transitions from 2*s*/2*p* electrons of Fe and Zn ions to fill 1*s* holes give rise to the corresponding emission lines in Fig. 2. The breaking-down of dipole-selection rule for the $2s \rightarrow 1s$ transitions is caused by non-spherical character in the 2s state due to density-induced distortions. Finally, the emission from transitions of continuum to the 1*s* hole can also be explained.

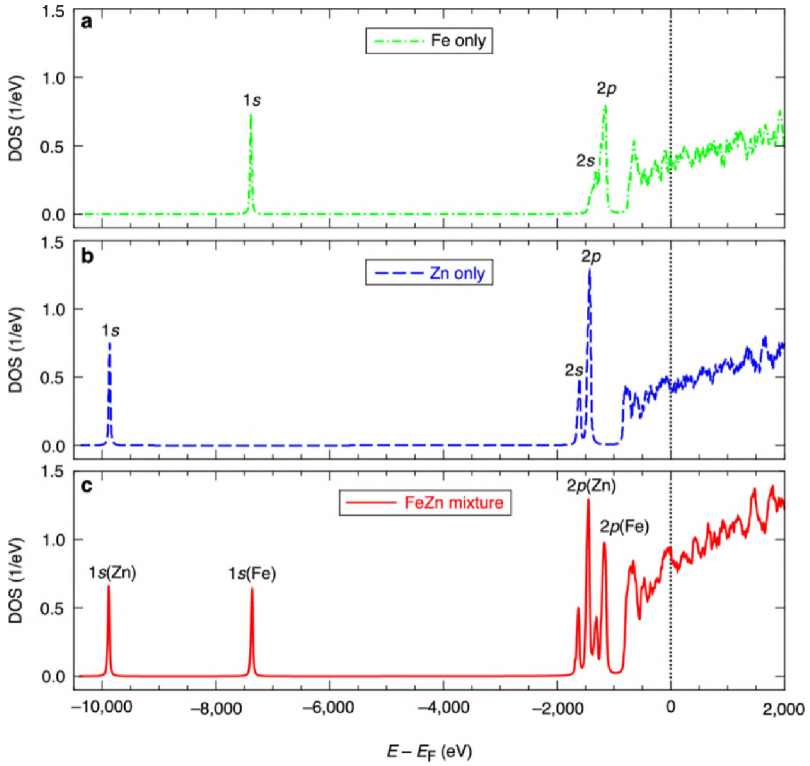

Fig. 3 **The density of states (DOS) of superdense plasmas. a** pure Fe plasmas, **b** pure Zn plasmas, and **c** Fe–Zn mixture plasmas at the same density and temperature of ρ = 1000 g cm^{-3} and kT = 50 eV.

Density dependence of interspecies radiative transition (IRT). To explore how density change affects the interspecies radiative transition in superdense plasmas, we have performed similar first principles calculations by varying the Fe–Zn density from ρ = 250 g cm^{-3} to ρ = 2000 g cm^{-3} but keeping kT = 50 eV. The DFT-predicted emission spectra are plotted in Fig. 4 for three different Fe–Zn plasma densities of ρ = 500, 1000, and 1500 g cm^{-3}. Again, the IRT peaks are highlighted by the dashed ellipses in each panel of the figure.

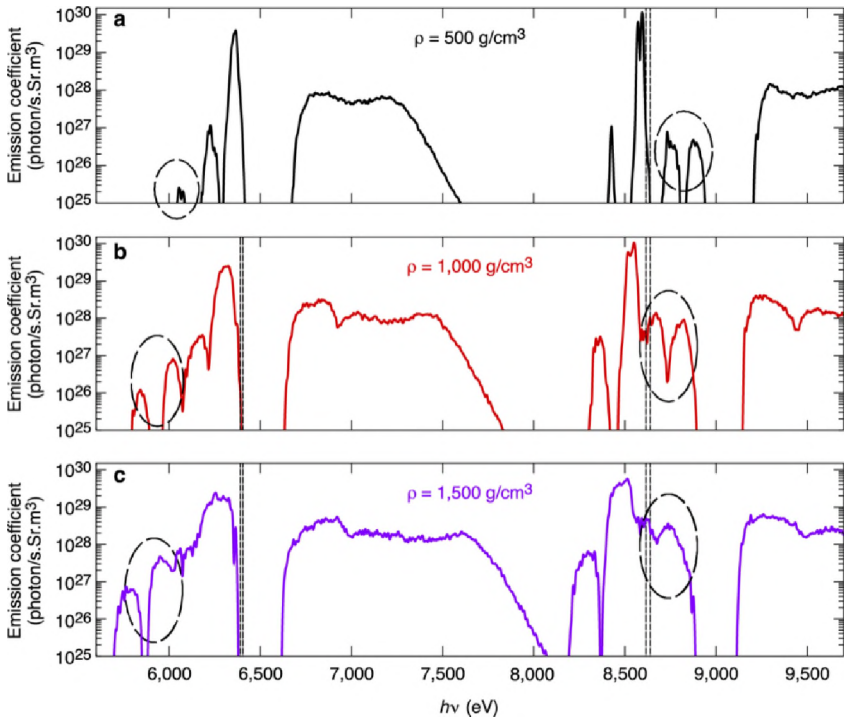

Fig. 4 **Interspecies radiative transitions (IRT) versus plasma density.** DFT calculations are done for superdense Fe–Zn mixtures at kT = 50 eV but different plasma mass densities: **a** $\rho = 500$ g cm^{-3}, **b** $\rho = 1000$ g cm^{-3}, and **c** $\rho = 1500$ g cm^{-3}.

At a relatively lower density of $\rho = 500$ g cm^{-3}, Fig. 4(a) shows that the interatomic K_α emission is significantly weaker than the normal intra-atomic K_α emission by ~3 to 4 orders of magnitude. They are even lower than that of dipole-forbidden intra-atomic $2s \rightarrow 1s$ transitions. It is noted that the spin-orbit coupling–induced splitting of $K_{\alpha 1}$ and $K_{\alpha 2}$ is clearly seen for Zn, but for Fe they are merged into one peak because of density/temperature broadenings. As the Fe–Zn plasma density increases to $\rho = 1000$ g cm^{-3} and $\rho = 1500$ g cm^{-3}, the interatomic K_α emission peaks drastically rise in amplitude and their widths increase as a result of strong density broadening [Figs. 4(b) and 4(c)]. At an extremely high Fe–Zn density of $\rho = 1500$ g cm^{-3},

Fig. 4(c) indicates that the peak amplitude of interatomic K_α from $2p$(Fe) → $1s$(Zn) transition can approach ~10% of the intra-atomic K_α from $2p$(Zn) → $1s$(Zn) transition, which should be readily detectable in experiments. It is noted that these interatomic transitions become even stronger than the dipole-forbidden intra-atomic $2s$(Zn) → $1s$(Zn) transition.

One interesting feature seen in Fig. 4 is that the interatomic K_α emission from $2p$(Fe) → $1s$(Zn) transition is always stronger than that of $2p$(Zn) → $1s$(Fe). To further explore this asymmetry and the overall trend of IRT versus plasma density, we have plotted the DFT-predicted ratio of the interatomic K_α signal $K_\alpha^{Zn\to Fe}$ or $K_\alpha^{Fe\to Zn}$ to the corresponding intra-atomic emission K_α^{Fe} (or K_α^{Zn}) (by the red diamond symbols in Fig. 5) as a function of interatomic distance between Fe and Zn ions. For a chosen Fe–Zn plasma density varying from ρ = 250 g cm^{-3} to ρ = 2000 g cm^{-3} at the same temperature of kT = 50 eV, we derived the Fe–Zn distance (d) from the orbital-free DFT-MD runs, in which *d* corresponds to the peak location of the pair distribution function—g(r). The full width half maximum of g(r) peak gives the plausible range of Fe–Zn distance ("error bar" of d in Fig. 5).

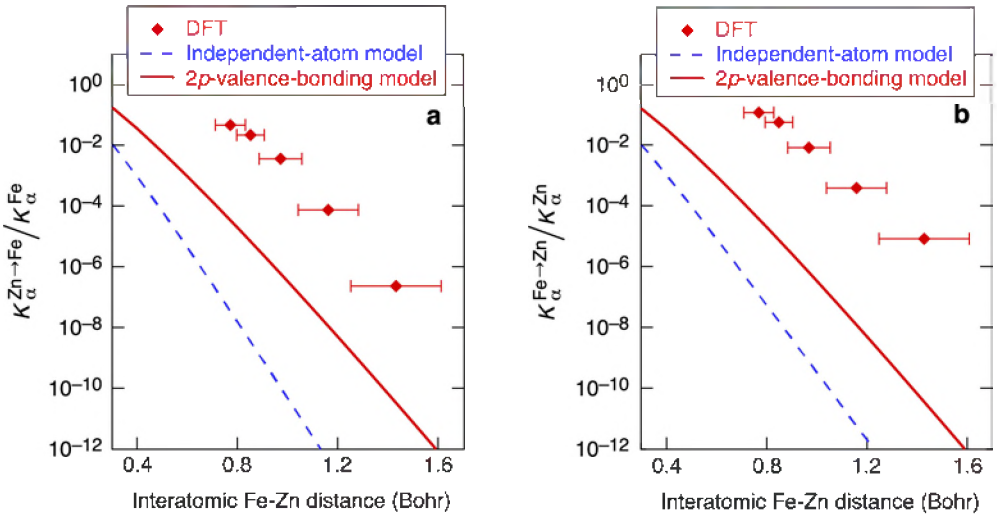

Fig. 5 **Model predictions of IRT in comparison with DFT calculations. a** The ratio of inter-atomic K_α emission (from Zn to Fe) to the regular intra-atomic K_α signal (within Fe) as a function of interatomic Fe-Zn distance. **b** Similar to **a** but for inter-atomic K_α emission from Fe to Zn. All of these calculations were done at different plasma densities with the same temperature of kT = 50 eV. DFT stands for density functional theory. The "error bar" in DFT data represents the full width half maximum of g(r) peak.

To further see how the interatomic K_α emission qualitatively changes with d, we have used two simple models to estimate the inter-to-intra K_α ratio through the following dipole-matrix elements calculations:

$$\frac{K_\alpha^{Zn(Fe)\to Fe(Zn)}}{K_\alpha^{Fe(Zn)}} = \frac{\left|\int_0^\infty \left\langle \psi_{final}^{model}(\mathbf{r})\left|\mathbf{e}.\mathbf{r}\right|\psi_{initial}^{model}(\mathbf{r}-\mathbf{d})\right\rangle d\mathbf{r}\right|^2}{\left|\int_0^\infty \left\langle \psi_{1s}^{Fe(Zn)}(\mathbf{r})\left|\mathbf{e}.\mathbf{r}\right|\psi_{2p}^{Fe(Zn)}(\mathbf{r})\right\rangle d\mathbf{r}\right|^2} \qquad (1)$$

where the unit vector **e** defines the direction of dipole moment. Depending on how we choose the initial and final states in the nominator of the above equation to estimate the

matrix element, we have two simple models: (a) the independent-atom model (IAM) which simply takes the *2p* and *1s* hydrogenic wave functions of independent Fe and Zn atoms as the initial and final states (namely $\left|\psi_{\text{initial}}^{\text{IAM}}(\mathbf{r})\right\rangle = \left|\psi_{2p}^{\text{Zn(Fe)}}(\mathbf{r})\right\rangle$ and $\left|\psi_{\text{final}}^{\text{IAM}}(\mathbf{r})\right\rangle = \left|\psi_{1s}^{\text{Fe(Zn)}}(\mathbf{r})\right\rangle$) ; and (b) the 2p-valence-bonding model in which the initial and final states have a form of symmetrized products of hydrogenic 1*s* and 2*p* wavefunctions of both Fe and Zn atoms, that is, $\left|\psi_{\text{initial}}^{\text{2p-valence-bonding}}(\mathbf{r}_1,\mathbf{r}_2)\right\rangle = \left[\left|\psi_{2p}^{\text{Fe}}(\mathbf{r}_1)\right\rangle\left|\psi_{2p}^{\text{Zn}}(\mathbf{r}_2)\right\rangle + \left|\psi_{2p}^{\text{Fe}}(\mathbf{r}_2)\right\rangle\left|\psi_{2p}^{\text{Zn}}(\mathbf{r}_1)\right\rangle\right]/\sqrt{2}$ and $\left|\psi_{\textit{final}}^{\text{2p-valence-bonding}}(\mathbf{r}_1,\mathbf{r}_2)\right\rangle = \left[\left|\psi_{1s}^{\text{Fe(Zn)}}(\mathbf{r}_1)\right\rangle\left|\psi_{2p}^{\text{Zn(Fe)}}(\mathbf{r}_2)\right\rangle + \left|\psi_{1s}^{\text{Fe(Zn)}}(\mathbf{r}_2)\right\rangle\left|\psi_{2p}^{\text{Zn(Fe)}}(\mathbf{r}_1)\right\rangle\right]/\sqrt{2}$ which is analog to the covalent bonding in molecules. For the latter model, six-dimensional integration over $\mathbf{r}_1$ and $\mathbf{r}_2$ is needed for evaluating the dipole matrix. Using these two models we can qualitatively estimate the above ratios as a function of the interatomic distance *d*. The results are plotted as the dashed-blue and solid-red lines in Figs. 5(a) and 5(b), respectively for the independent-atom model and the 2p-valence-bonding model. One can see that these simple models qualitatively give the overall trend of increasing interatomic K_α emission as interatomic distance decreasing; Quantitatively, both models show orders of magnitude differences from many-body DFT calculations. Nevertheless, the 2p-valence-bonding model is better than the independent-atom model, which manifests the molecular-bonding nature among atoms in such super-dense systems. Molecular bonding involving more than two atoms might account for the discrepancies between the two simple models and DFT calculations. It is noted that the multicenter wave-function nature[37] was properly accounted for by DFT. At the highest density

explored (ρ = 2000 g cm^{-3}), Fig. 5(b) shows that the interatomic $K_{\alpha}^{Fe\rightarrow Zn}$ emission can reach over 11% of the regular intra-atomic K_{α}^{Zn} signal. The asymmetry that the interatomic K_{α} emission from $2p$(Zn) → $1s$(Fe) transition is always weaker than that of $2p$(Fe) → $1s$(Zn) is caused by the fact that the $2p$ state of Fe ion $\left[\left|\psi_{2p}^{Fe}(\mathbf{r})>\right.\right]$ spreads much more than $\left|\psi_{2p}^{Zn}(\mathbf{r})>\right.$ (because the former is less bounded) so that it can have significant overlap with the *1s* hole of Zn (see Fig. 1). This consideration is further confirmed by looking into the orbital (wave-function) overlap in such superdense situations.

Finally, we shall discuss the radiative-to-nonradiative decay branching ratio for 1s-core-hole states created in such super-dense plasma mixtures. We shall point out that for super-dense plasmas considered here, the nonradiative Auger decay channel is hard to measure because Auger electrons will quickly thermalize inside the super-dense plasma; On the other hand, the radiative decay can be easily probed by measuring the escaped K_{α} photons through spectrometers. To calculate the ratio of K_{α} emission to Auger decay, we have used the atomic kinetic modeling code PrimSPECT[38] which is extensively used in the plasma physics community. For the concerned plasma densities varying from 250- g cm^{-3} to 2000 g cm^{-3} and kT=50-eV, the averaged ionizations of Fe and Zn ions are about <Z>=15.8~16.2 and <Z>=19.5~20.1, respectively. Namely, such super-dense plasmas mainly consist of neon-like ions of Fe^{16+} and Zn^{20+}, which both have the dominant electronic configuration of $1s^2 2s^2 2p^6$ that is close to what is shown by Fig. 3. Now, if external radiative/collisional pump creates 1s-core-hole state ($1s^1 2s^2 2p^6$) of both ions, we

can use PrimSPECT to compute the decay rate coefficients. The calculations give a decay rate of $\Gamma_{rad} = 5.4 \times 10^{14}\ s^{-1}$ for the radiative channel of $1s^1 2s^2 2p^6 \rightarrow 1s^2 2s^2 2p^5$ (K_α emission) for Fe^{17+} ions, while its Auger decay rate is about $\Gamma_{Auger} = 9.8 \times 10^{14}\ s^{-1}$ for the dominant transition of $1s^1 2s^2 2p^6 \rightarrow 1s^2 2s^2 2p^4$. Thus, the radiative-to-Auger branching ratio for Fe^{17+} ions is about $\Gamma_{rad}/\Gamma_{Auger} \approx 0.55$. For Zn^{21+} ions, PrimSPECT calculations give the two decay rate coefficients of $\Gamma_{rad} = 1.01 \times 10^{15}\ s^{-1}$ and $\Gamma_{Auger} = 1.07 \times 10^{15}\ s^{-1}$, respectively, which results in a branching ratio of $\Gamma_{rad}/\Gamma_{Auger} \approx 0.94$. These calculations indicate that the radiative decay channel has the same order of probability as the nonradiative Auger decay for intra-atomic transitions. In other words, one third of Fe^{17+} core-hole ions will decay radiatively, while one half of Zn^{21+} core-hole ions will emit K_α photons through intra-atomic transitions. Given the same physics nature of radiative versus nonradiative decay for both intra-atomic and inter-atomic transitions, we expect the similar branching ratio should hold between the inter-atomic radiative transition and the inter-atomic Coulombic decay[39-41]. Once again, the inter-atomic Coulombic decays[39-41] certainly occur within such super-dense plasmas, although they may not be measured as easily as the inter-atomic radiative transitions.

Possible experiments on inter-atomic K_α emissions. Experimental verification of these first-principles predictions of interatomic K_α emissions can possibly be conducted at the Omega Laser Facility utilizing the platform of double-shell implosions[14,15,42,43]. In a double-shell target, the inner metal shell can be made of mid-Z Fe-Cu or Fe-Zn alloys with a core of D_2-gas fill. When a low-Z outer shell

(beryllium or polystyrene) is driven symmetrically by the 60-beam OMEGA laser to spherically impact on the inner shell, it can cause the inner Fe–Zn (or Fe–Cu) shell to implode. A small convergence ratio of $CR = R_{initial}/R_{final} \sim 8$ to 10 of the metal shell could give rise to a mass density of ρ = 500 to 2000 g cm^{-3} for the inner Fe–Zn (or Fe–Cu) shell at its stagnation[42,43]. To create the 1*s* holes of Fe and Zn/Cu ions, one option is to use the high-intensity OMEGA EP beam to generate MeV electrons that can remove some of the 1*s* electrons of Fe and Zn/Cu ions through collisions. The other option is to fill the double-shell target with mid-*Z* gases such as Ar and Kr. As a result, the hot-spot self-emission with a certain amount of hard x-rays could ionize the 1*s* electrons of Fe and Zn/Cu ions by radiation pumping. The latter method has been successfully demonstrated in single-shell implosions on OMEGA. In both ways, the created hollow Fe/Zn/Cu ions in such extremely dense plasmas will give rise to interatomic K_α emissions, as we have predicted here. These interatomic K_α emissions can be measured by spectrometers with a dynamic range of 100 to 1000.

Discussions

The two phenomena predicted from our first principles DFT calculations, which are the interspecies radiative transition and the breaking down of dipole selection rule in extremely dense plasma mixtures, can have significant implications to high-energy-density (HED) science, ICF, and astrophysics. For plasma opacity/emissivity calculations, the cross-talking between different species and dipole-forbidden transitions have generally been ignored so far by the HED science community. Our first-principles results

show that these inter-atomic radiative transitions can become significant and even comparable with normal intra-atomic transitions. The overall trend of IRT can be qualitatively understood by the independent atom model and the 2p-valence-bonding model; while transient multi-atom molecular bonding could account for the enhancement of IRT in superdense plasmas. One would expect that these emission/absorption channels, opened up in the warm and extremely dense regime, could affect the radiation transport in ICF (e.g., double-shell targets) and astrophysical objects such as brown-dwarf cores. It is noted that the interatomic radiative transitions shall occur in superdense single-species plasmas, although they might be indistinguishable to the normal intra-atomic transitions.

Methods

Our DFT calculations were performed with the ABINIT software package[33,34] in which electrons are treated quantum-mechanically with a plane-wave finite-temperature Kohn-Sham DFT description. The electrons and ions are in thermodynamic equilibrium with an equal temperature ($T_e = T_i$). The electron–nucleus interaction is described in the projector augumented-wave (PAW) approach by a pseudopotential generated with a very small matching radius ($r_c = 0.2$ bohr). All electronic wave-functions are explicitly computed in the thermal DFT formalism. For the electronic exchange and correlation interactions we use the generalized gradient approximation (GGA) with the Perdew–Burke–Ernzerhof (PBE) functional[44]. It is noted that the PBE functional has been widely used in DFT calculations for warm-/hot-dense plasmas[45-48] that showed good agreements with HED experiments; Our results presented here are insensitive to the choice of exchange-correlation functional, for which the local-density approximation (LDA) gives essentially

identical results except for small energy shifts (see Supplementary Information). To sample the dense plasma configurations, we have conducted molecular-dynamics simulations based on orbital-free DFT. Namely, under the Born–Oppenheimer approximation, the self-consistent electron density is first determined for an ion configuration. Then, the classical ions are moved by the combined electronic and ionic forces, using Newton's equation. This molecular-dynamics procedure is repeated for thousands of time steps, from which optical property (x-ray emission/absorption) can be directly evaluated. Note that we have applied the periodic boundary condition to our first-principles calculations, with a box size determined by the Fe–Zn density and the number of atoms used. Convergent results for K_α emissions were reached by using 32 atoms in a super cell, the Baldereschi mean value point for the Brillouin zone sampling[49], and the highest plane-wave energy cutoff of $E_{cut} \approx 68$ keV. This high-energy cutoff is necessary to accurately sample the deeply bound 1*s* core electrons. Detailed convergence tests can be found in the Supplementary Information.

After we ran the calculations for thousands of OFMD steps, we obtained a sufficiently long trajectory of ionic configurations. We then chose several uncorrelated snapshots from these ionic configurations to calculate the x-ray emission spectra of dense Fe–Zn plasmas by using the Kubo–Greenwood formalism[50,51]. Because of the underestimated band gap by the PBE-functional due to electron self-interaction, the resulting spectra were shifted by a constant of $\delta\omega \approx 110$ eV (~1.5% of the 1*s*–2*p* bandgap) to match the K_α locations of ambient Fe and Zn. This is justified by comparing the Hartree–Fock calculated energy 1*s*–2*p* gap with the PBE-DFT results. The similar

matching technique has shown to work well for the measured K_α emission in warm dense Cu experiments on OMEGA EP.

In the K_α-emission calculations, the dipole approximation has been invoked. For the concerned photon energy range of hν=6.0~8.8 keV, the corresponding electromagnetic waves have wavelengths of $\lambda \approx 1.4 \sim 2.1$ Å (2.6~3.97 Bohr). Taking an isolated Fe atom as an example, Hartree-Fock calculations give a size of *2s* and *2p* states (<2s|r|2s> or <2p|r|2p>) about ~0.12-0.14 Å, which is one order of magnitude smaller than the wavelength of K_α emissions so that the dipole approximation holds well for intra-atomic transitions. For inter-atomic K_α emissions in super-dense Fe-Zn plasmas ($\rho \geq$ 1000 g cm^{-3}) concerned here, the inter-atomic Fe-Zn distance is around d=0.8~1.0 Bohr. Taking this emitting entity of Fe-Zn as a whole, its size is still about ~3-5 times smaller than the K_α wavelength. Nevertheless, this prompts us to consider high-order contributions such as the electric quadrupole emission, which is examined by computing the contribution of electric quadrupole term with the independent-atom model for different densities (*i.e.*, different inter-atomic Fe-Zn distances). The results indicated that the relative contribution ratio of quadrupole to dipole is overall less than ~3.2% (see Supplementary Information).

Acknowledgment and Disclaimer

This material is based upon work supported by the Department of Energy National Nuclear Security Administration under Award Number DE-NA0003856, the University of Rochester, and the New York State Energy Research and Development

Authority. This work is partially supported by US National Science Foundation PHY Grant No. 1802964 for SXH and VVK.

Data availability. The data that support the findings of this study are available from the corresponding author upon request. They can be immediately shared through email or any other file-sharing systems.

Code availability. The codes for K_α-emission calculations and IRT models are available from the corresponding author upon request.

Author Contributions: S.H. conceived the project, performed the DFT calculations, and wrote the initial manuscript. V.V.K. created the all-electron PAW pseudopotentials and modified the ABINIT absorption code to calculate emission spectra. V.R., N.B., and

M.T. have implemented the spin-orbital calculation for optical properties in ABINIT and provided the code and help on running it. P.M.N. and S.X.H. discussed the possible experimental designs. All authors discussed the results and revised the manuscript.

Competing interests: The authors declare no competing interests.

References

1. Burrows, A., Hubbard, W.B., Lunine, J.I., Liebert, J., The theory of brown dwarfs and extrasolar giant planets. *Rev. Mod. Phys.* 73, 719–765 (2001).
2. Fontaine, G., Brassard, P. & Bergerson, P. The potential of white dwarf cosmochronology. *Publ. Astron. Soc. Pacif.* 113, 409–435 (2001).
3. Tremblay, P.-E. *et al.* Core crystallization and pile-up in the cooling sequence of evolving white dwarfs. *Nature* 565, 202–205 (2019).
4. Campbell, E. M. and Hogan, W. J. The National Ignition Facility – applications for inertial fusion energy and high-energy-density science. *Plasma Phys. Control. Fusion* **41**, B39 (1999).
5. Batani, D. *et al.* Development of the PETawatt Aquitaine Laser system and new perspectives in physics. *Phys. Scripta* **T161**, 014016 (2014).
6. Miquel, J.-L. and Prene, M. LMJ & PETAL status and program overview. *Nucl. Fusion* **59**, 032005 (2019).
7. Rose, S. J. New experimental possibilities for measuring radiative opacity under conditions in the sun's interior. *Plasma Phys. Control. Fusion* **47**, B735–B741 (2005).
8. Matzen, M. K. *et al.* The refurbished Z facility: capabilities and recent experiments. *Acta Phys. Pol.* A 115, 956 (2009).
9. Doeppner, T. *et al.* Demonstration of high performance in layered deuterium–tritium capsule implosions in uranium hohlraums at the National Ignition Facility. *Phys. Rev. Lett.* **115**, 055001 (2015).

10. Regan, S. P. *et al.* Demonstration of fuel hot-spot pressure in excess of 50 Gbar for direct-drive, layered deuterium-tritium implosions on OMEGA. *Phys. Rev. Lett.* **117**, 025001 (2016).

11. Le Pape, S. *et al.* Fusion energy output greater than the kinetic energy of an imploding shell at the National Ignition Facility. *Phys. Rev. Lett.* **120**, 245003 (2018).

12. Doeppner, T. *et al.* Absolute equation-of-state measurement for polystyrene from 25 to 60 Mbar using a spherically converging shock wave. *Phys. Rev. Lett.* **121**, 025001 (2018).

13. Gopalaswamy, V. *et al.* Tripled yield in direct-drive laser fusion through statistical modelling, Nature **565**, 581-586 (2019).

14. Amendt, P. *et al.* Indirect-drive noncryogenic double-shell ignition targets for the National Ignition Facility: design and analysis. *Phys. Plasmas* **9**, 2221 (2002).

15. Ping, Y. *et al.* Enhanced energy coupling for indirectly driven inertial confinement fusion. *Nat. Phys.* **15**, 138-141 (2018).

16. Ciricosta, O. *et al.* Direct measurements of the ionization potential depression in a dense plasma. *Phys. Rev. Lett.* **109**, 065002 (2012).

17. Hoarty, D. J. *et al.* Observations of the effect of ionization-potential depression in hot dense plasma. *Phys. Rev. Lett.* **110**, 265003 (2013).

18. Hu, S. X. Continuum lowering and Fermi-surface rising in strongly coupled and degenerate plasmas, *Phys. Rev. Lett.* **119**, 065001 (2017).

19. Hansen, S. B. *et al.* Fluorescence and absorption spectroscopy for warm dense matter studies and ICF plasma diagnostics. *Phys. Plasmas* **25**, 056301 (2018).

20. Nilson, P. M. *et al.* Time-resolved measurements of hot-electron equilibration dynamics in high-intensity laser interactions with thin-foil solid targets. *Phys. Rev. Lett.* **108**, 085002 (2012).

21. Smid, M. *et al.* Characterization of suprathermal electrons inside a laser accelerated plasma via highly-resolved Kα-emission. *Nat. Commun.* **10**, 4212 (2019).

22. Rose, S. J. Calculations of the radiative opacity of laser-produced plasmas. *J. Phys. B* **25**, 1667 (1992).

23. Iglesias, C. A., Rogers, F. J. Updated OPAL Opacities. Astrophys. J. 464, 943 (1996).

24. Rose, S. J. The radiative opacity at the Sun centre—a code comparison study. *J. Quant. Spectro. Rad. Trans.* **71**, 635-638 (2001).

25. Blancard, C., Cosse, P., Faussurier G. Solar mixture opacity calculations using detailed configuration and level accounting treatments. *Astrophys. J. 745*, 10 (2012).

26. Colgan, J. *et al.*, A new generation of Los Alamos Opacity Tables. *Astrophys. J.* **817**, 116 (2016).

27. Cederbaum, L. S., Zobeley, J., Tarantelli, F., Giant intermolecular decay and fragmentation of clusters. Phys. Rev. Lett. 79, 4778 (1997).

28. Schwartz, G. P., Fatehi, S., Saykally, R. J., Prendergast, D., Importance of Electronic Relaxation for Inter-Coulombic Decay in Aqueous Systems. *Phys. Rev. Lett.* **105**, 198102 (2010).

29. Rudenko, A. *et al.* Femtosecond response of polyatomic molecules to ultra-intense hard X-rays. *Nature* **546**, 129 (2017).

30. Lapp, M. Collision enforced transitions in cesium. *Phys. Lett.* **23**, 553–554 (1966).

31. Gallagher, Alan & Holstein, T. Collision-induced absorption in atomic electronic transitions. *Phys. Rev. A* **16**, 2413–2431 (1977).

32. Ueda, K., Komatsu, T. & Sato, Y. Observation of collision-induced- dipole absorption bands in strontium–rare gas mixtures. I. The 5s–4d bands. *J. Chem. Phys.* **91**, 4495–4498 (1989).

33. Gonze, X. *et al. Recent developments in the ABINIT software package. Comput. Phys. Commun.* **205**, 106-131 (2016).

34. Torrent, M., Jollet, F., Bottin, F., Zérah, G. & Gonze, X. Implementation of the projector augmented-wave method in the ABINIT code: Application to the study of iron under pressure. *Comp. Mater. Sci.* **42**, 337–351 (2008).

35. Lambert, F., Clérouin, J., Zérah, G., Very-high-temperature molecular dynamics. *Phys. Rev. E* **73**, 016403 (2006).

36. Recoules, V., Lambert, F., Decoster, A., Canaud, B., Clérouin, J., *Ab Initio* determination of thermal conductivity of dense hydrogen plasmas. *Phys. Rev. Lett.* 102, 075002 (2009).

37. Rose, S. Two-center electronic wave functions in plasmas. *J. de. Physique Colloques* **44(C8)**, 159 (1983).

38. MacFarlane, J. J., Golovkin, I. E. *et al.* Simulation of the ionization dynamics of aluminum irradiated by intense short-pulse lasers, in: Proceedings of Inertial

Fusion and Science Applications 2003, American Nuclear Society, LaGrange Park IL, 2004.

39. Averbukh, V. & Cederbaum, L. S. Interatomic electronic decay in endohedral fullerenes. *Phys. Rev. Lett.* 96, 053401 (2006).

40. Averbukh, V., Saalmann, U., Rost, J. M. Suppression of Exponential Electronic Decay in a Charged Environment. *Phys. Rev. Lett.* 104, 233002 (2010).

41. Cooper, B. & Averbukh, V. Single-Photon Laser-Enabled Auger Spectroscopy for Measuring Attosecond Electron-Hole Dynamics. *Phys. Rev. Lett.* **111**, 083004 (2013).

42. Montgomery, D. S. *et al.* Design considerations for indirectly driven double shell capsules. *Phys. Plasmas* **25**, 092706 (2018).

43. Hu, S. X. *et al.* Direct-drive double-shell implosion: A platform for burning-plasma physics studies. *Phys. Rev. E* **100,** 063204 (2019).

44. Perdew, J. P., Burke, K. & Ernzerhof, M. Generalized gradient approximation made simple. *Phys. Rev. Lett.* 77, 3865–3868 (1996).

45. Pickard, C. J. & Needs, R. J. Aluminium at terapascal pressures. *Nature materials **9**, 624 (2010).*

46. Vinko, S. M., Ciricosta, O. & Wark, J. S. Density functional theory calculations of continuum lowering in strongly coupled plasmas. *Nature Communications* **5**, 3533 (2014).

47. *Davis, P. et al.,* X-ray scattering measurements of dissociation-induced metallization of dynamically compressed deuterium. *Nat. Communications 7, 11189 (2016).*

48. *Döppner, T. et al.,* Absolute Equation-of-State Measurement for Polystyrene from 25 to 60 Mbar Using a Spherically Converging Shock Wave. *Phys. Rev. Lett.* ***121****, 025001 (2018).*

49. Baldereschi, A. Mean-value point in the Brillouin zone. *Phys. Rev. B* **7**, 5212–5215 (1973).

50. Kubo, R. Statistical-mechanical theory of irreversible processes. I. General theory and simple applications to magnetic and conduction problems. *J. Phys. Soc. Jpn.* **12**, 570-586 (1957).

51. Greenwood, D. A. The Boltzmann equation in the theory of electrical conduction in metals. *Proc. Phys. Soc. Lond.* **71**, 585–596 (1958).